Aerodynamic fragmentation of water, ethanol and polyethylene glycol droplets investigated by high-speed in-line digital holography

Zacaria Essaïdi, Pierre Lauret, Frederic Heymes, Laurent Aprin, Pierre Slangen

Aerodynamic fragmentation of water, ethanol and polyethylene glycol droplets investigated by high-speed in-line digital holography

Zacaria Essaïdi [a,*], Pierre Lauret [a], Fréderic Heymes [a], Laurent Aprin [a], Pierre Slangen [b]

[a] Laboratoire des Sciences des Risques (LSR), IMT Mines Ales, Ales, France
[b] EuroMov Digital Health in Motion, Univ Montpellier, IMT Mines Ales, Ales, France

A B S T R A C T

Digital holography is a remarkable interferometric technique for determining the size, shape, distribution, and spatial location of particles. Therefore, when combined with high-speed imaging technology, it represents a relevant technique for the study of the aerodynamic fragmentation phenomenon wherein the aerodynamic strengths counterbalance the cohesion forces of the drops causing thus their decomposition. We discuss in this paper the droplets fragmentation of water, ethanol and polyethylene glycol 300 solutions interacting with a shock wave and flow generated by an open-ended shock tube. In this context, a shock tube device was set up, and both the released flow as well as the shock wave generated were characterized by ultrafast imaging shadowgraphy and high speed pressure measurement. Millimeter diameter average drops are fragmented and imaged by high-speed digital in-line holography at a rate of 24800 fps, and then the image retrieved numerically. The Weber numbers are determined for each liquid and the observed fragmentation patterns are consistent with the description of the 'chaotic regime' reported in the literature by Pilch and Erdman (1987) [1].

Keywords:
Liquids fragmentation
Aerodynamic fragmentation
In-line digital holography
Shock tube
High-speed imaging

1. Introduction

Optical digital holography is a two-steps interferometric imaging technique enabling a simultaneous recording of the amplitude and the phase of a wave diffracted by an object and it reconstruction. The holograms are recorded either on CMOS or on CCD sensors and numerically processed. Such a tool is therefore highly attractive for applications in the field of fluids mechanics that often require non-intrusive diagnoses. Both qualitative and qualitative restitutions of 3D structures of complex flows are made possible thanks to specific algorithms and experimental setups [2–5]. Two categories of holographic setups have to be distinguished: The in-line holography and the off-axis holography. The digital in-line holography also known as Gabor holography was the first one introduced [6] and refers to the case wherein the reference and object interfering beams are collinear. The objects are reconstructed with a high resolution which nevertheless are stained with an overlap of additional signals (twin-image and zero-order contributions) [7]. To overcome this limitation, few years later, the off-axis configuration wherein the reference beam is slightly tilted (reference and object beams are not parallel) was proposed by Leith and Upatnieks [8]. This ensures a filtering within the object reconstruction process since the terms expressing the object, the zero order and the conjugate object are separated in the spatial frequency domain. Though, acting this way, the bandwidth of the reconstruction is substantially limited. Hence, the experimental setups are therefore adapted according to the investigations requirements.

When dealing with particles analysis, the in-line holography is of high interest since it allows determining their size, shape, and spatial location. This method is also suitable because of its simplicity of implementation and insensitivity to vibrations. This technique is therefore relevant to investigate the aerodynamic fragmentation of liquids drops wherein the inertial forces of the flow counterweight the cohesive forces of the drops causing their deformation and decomposition. The understanding and the control of aerodynamic breakup is important because of the resulting wide variety of applications: in: agriculture, diesel engines, combustion, aerospace …

We are interested on aerodynamic breakup phenomenon because it can occur in scenarios of particular risks [9,10] or for the mitigation of the effects of explosions by water curtains. In the presence of industrial tanks with leaks followed by an explosion, it is important to understand and properly estimate generated droplet properties for better risk management.

* Corresponding author.
E-mail address: zessaidi@gmail.com (Z. Essaïdi).

In this paper, we investigate and discuss the aerodynamic fragmentation of 3 newtonian liquids (ethanol, water and polyethylene glycol) interacting with the shock wave and the flow field produced by a shock tube. For this purpose, a small open-ended shock-tube is designed and fully characterized to be adapted to the optical lab scale. The aerodynamic breakup is investigated by means of the high speed in-line digital holography, sometimes called time-resolved digital holography.

2. Materials and methods

2.1. Shock tube characterization and ultra-fast flow visualization

A cylindrical open-ended shock tube with a 63 mm inner diameter was developed to adapt the aerodynamic fragmentation of liquids drops at the laboratory scale. It consists of a 700 mm length high pressure chamber (driver section) and a 300 mm length expansion chamber (driven section) separated by a membrane made of 20 μm thick aluminum foils. The high pressure chamber is filled by air and the pressure within is increased till the membrane rupture causing the instantaneous release of the compressed fluid and a shock wave generation. The amplitude of the generated shock wave can be tuned by adjusting the number of aluminum foils. For the current experiment, 4 aluminum foils were gathered and used as a single membrane. The overpressure was measured by a pressure sensor (PCB 137A23 type) placed at a distance $d_{ts} = 297$ mm on the propagation axis from the shock tube outlet. High speed data acquisition is carried out with 2 MHz sampling by means of fast data acquisition device (HBM Gen7).

The produced flow is visualized by means of shadowgraph imaging technique which is sensitive to the second order derivative of the refractive index of the fluid [11,12]. The latter is related to it density through the Gladstone Dale relation [11,13]. Basically, within this technique, the flow is illuminated with parallel beams stemming from the spatially filtered and expanded laser beam or a punctual broadband light source, which is then recorded with a camera. Without flow the camera sensor records a uniform enlightenment whereas with a flow, the variations of the fluid density induces refractive index changes that phase shift or deflect the light passing through the fluid. As results, intensity variations are observed in the recorded signal. This technique is widely exploited in fluid mechanics filed [12] and will not be detailed further in this paper. In our experiment, as light source a coherent and continuous laser (Coherent, Verdi V5) was used and the shadowgraphs were recorded with a high speed CMOS camera (Vision Research Phantom, V2512 camera) with a magnification × 9 (Tamron Objective AF 70–300 mm) at a rate of 31000 frames per second. The laser power was set to 200 mW, the exposure time of the camera to 2 µs.

2.2. Digital in-line holography setup

The digital in-line holographic setup is depicted in Fig. 1. It consists of a continuous coherent source (CNI laser, model MSL-III-532) emitting at the wavelength $\lambda = 532$ nm with a maximum power of 50 mW and a CMOS detector (Phantom, VEO 710 camera) made of 1280 × 800 square pixels of 20 µm side. Images can be recorded at a frame rate of 7400 frames per second at full resolution; however, this frame rate can be increased by reducing the size of the region of interest on the recorded images. To be able to follow the fragmentation phenomenon, the region of interest was cropped to 512 × 512 pixels which allows to reach 24800 fps and exposure time was set to 1 µs.

The intensity of the beam emitted by the laser is firstly adjusted using a density filter. Then, the beam is cleaned using a spatial filter composed of a microscope objective (Nikon, × 20, N.A. = 0.4) and a 25 μm

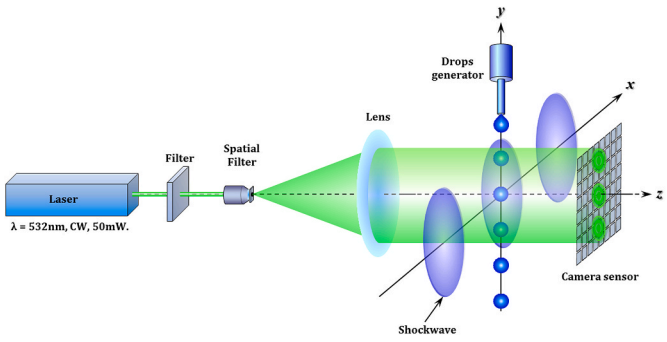

Fig. 1. Schematics of the in-line digital holography experimental setup.

diameter pinhole. The beam is thereafter collimated using a 500 mm convergent focal lens before being collected by the camera. A syringe, coupled with automatic dispenser, placed at a distance d_0 from the camera sensor allows generating a continuous stream of drops. The latter are then impacted by both the flow and the shock wave created by the open ended shock tube set perpendicularly to the optical path. The operating distance d_0 was adjusted ($d_0 \sim 33$ cm) in order to both avoid any potential damage that might occur on the camera due to the shock wave and to fulfil the critical sampling condition [14] for the numerical reconstruction distance given by $z = L.\Delta x/\lambda = 38.4$ cm. The light scattered by the drops (object wave O) interferes with the undisturbed one constituting the background (reference wave R) to form the holograms $h(x, y)$ that are recorded by the camera sensor plane. The resulting expression of the hologram is given by equation (1).

$$\begin{aligned} h(x,y) &= |O(x,y) + R(x,y)|^2 \\ h(x,y) &= (O(x,y) + R(x,y))(O(x,y) + R(x,y))^* \\ h(x,y) &= O(x,y)O^*(x,y) + R(x,y)R^*(x,y) + R(x,y)O^*(x,y) + O(x,y)R^*(x,y) \end{aligned} \tag{1}$$

where * denotes the complex conjugation.

2.3. Digital reconstruction and optimal reconstruction distance determination

The recorded holograms $h(x, y)$ are digitally processed by considering the scalar diffraction theory. Within the digital reconstruction process, the real image $O(x, y)$ is obtained by multiplying the hologram $h(x, y)$ by the reference $R(x, y)$ wave and back propagated to the reconstruction plane locate at a distance d_0 by means of propagator operator. In the current study, such propagation is achieved using the angular spectrum propagation method [15–17] given by equation (2).

$$O(x,y,z=d) = \boldsymbol{FT}^{-1}\{\boldsymbol{FT}[O(x,y,z=0)]\boldsymbol{H}(f_x,f_y)\} \tag{2}$$

where $\boldsymbol{H}$ is a transfer function:

$$\boldsymbol{H}(f_x,f_y) = \begin{cases} exp\left(i\frac{2\pi}{\lambda}d\sqrt{1-(\lambda f_x)^2-(\lambda f_y)^2}\right) & if \quad f_x{}^2+f_y{}^2 < \frac{1}{\lambda^2} \\ 0 \quad else \end{cases} \tag{3}$$

$\boldsymbol{FT}$ and $\boldsymbol{FT}^{-1}$ denote the Fourier Transform and it inverse transform respectively, d is the reconstruction distance, λ is the laser wavelength and f_x, f_y are the spatial frequencies.

Although the backpropagation process can be achieved by simply taking into account the experimental value of the reconstruction distance d_0, further numerical processing is carried out to allow an improvement of the detection of the spatial location of this

reconstruction plane. Several metrics for the refocus plane detection relying on the phase distribution [18–20], amplitude [21,22] of the reconstructed images or mix of these [23] are reported and discussed in the literature [24,25]. These metrics involve criteria such as the image derivative [26], it histogram [27], it autocorrelation function [28]. In our study, automatic detection of the optimal distance d_0 is reached by considering the sharpness of the liquid drops edges before their interaction with the shock wave. The image restitution process implies the whole image and can be reduced to emphasize specific objects. The quantification of the image sharpness relies on it derivative properties and is investigated over the [0 mm–500 mm] space propagation interval. The gradients are assumed to be higher when the distance d_0 is reached emphasizing thus the sharpness of the drop edges and decrease as we move away from it. Nevertheless, such approach requires good quality images since it is sensitive to the noise.

2.4. Liquids

Fragmentation properties of pure water, ethanol and polythylene glycol (PEG) solutions were investigated. The water (H_2O) is an ultra-purified water provided by a Milli-Q system with a surface tension of $\gamma_1 = 72.8 \times 10^{-3}$ N m^{-1}, a density of $\rho_1 = 1000$ kg m^{-3} and a viscosity of $\mu_1 = 1.00 \times 10^{-3}$ Pa s [29]. Both ethyl alcohol (C_2H_6O) and polyethylene glycol PEG ($H(OCH_2CH_2)_nOH$) were purchased from Sigma-Aldrich and have been used without any further modifications. Ethanol solution has a surface tension of $\gamma_2 = 22.1 \times 10^{-3}$ N m^{-1}, a density of $\rho_2 = 789$ kg m^{-3} and a viscosity of $\mu_2 = 1.20 \times 10^{-3}$ Pa s [30]. Finally, the PEG used has an average molecular weight (M) of 300 g mol^{-1}. It surface tension is $\gamma_3 = 44.5 \times 10^{-3}$ N m^{-1} it density $\rho_3 = 1125$ kg m^{-3} and it viscosity $\mu_3 = 95 \times 10^{-3}$ Pa s at 20 °C [31].

3. Results and discussions

3.1. Shock tube properties

Typical shock waves produced by the shock tube and propagating in the near field free atmosphere are fairly well described by the Friedlander function [32–34]. The so-called Friedlander function (ideal blast wave) exhibits an overpressure peak with a sharp rising front which decays exponentially then followed by a depression. Out of the shock tube, as the shock wave expands freely in opening space, the amplitude of the overpressure peak decreases quickly and the pressure signal degrades while moving away from the exit of the tube [35]. An example of the pressure - time profile measured on the shock tube axis at a distance $d_{ts} = 297$ mm from it exit is reported on Fig. 2. The time scale origin is set arbitrary. The pressure signal shows a complex shape with multiple peaks rather than the theoretical Friedlander curve. The first two peaks of 50 mbar belong to the same initial main shock wave that breaks down away from the shock tube exit. The forward additional peak is attributed to the compression of the air contained in the driven section and to it short length. Such peak disappears for sufficiently longer driven section length as the shock wave pressure profile evolve during its propagation within [33,36,37]. The overpressure stand to 95.5 mbar at a shorter distance $d_{ts} = 172$ mm. It is followed by a 23 mbar depression (−135.5 mbar at $d_{ts} = 172$ mm) others additional shocks. The isolated peak located at $t \sim 13$ ms corresponds to the reflection of the main shock wave by the floor. Also, at a distance $d_{ts} = 74$ mm from the shock tube exit where the test are performed, the liquids drops to be fragmented undergo a pressure variation of a few hundred mbar.

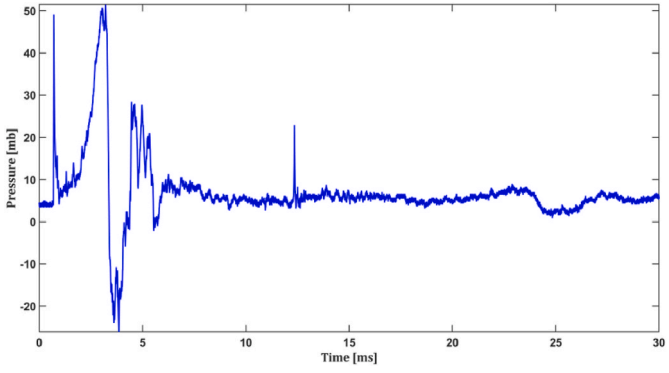

Fig. 2. Typical high speed pressure measurement carried at a distance $d_{ts} = 297$ mm from the exit of open-ended shock tube.

Typical experimental shadowgraph pictures of the shock tube output flow are reported on Fig. 3a. The shadowgraphs (159.3 mm × 106.0 mm) were recorded with a time interval of 32.25 μs and show the chronological evolution of the shock wave propagation and the vortex ring emergence. The large horizontal dark band corresponds to the shock tube and the vertical one to a second distant tube not involved here. As shown by the shadowgraphs, a planar shock wave appears at the exit of the shock tube ($t = 32.25$ μs) then propagates in the free space. Both forward and backward propagation are highlighted. The axial forward part of the wave velocity v_1 was extracted from these pictures by least squares regression of the spatial profile propagation and was find to be about 384 m s^{-1}. During the propagation, the shock wave remains flat over the entire section of the shock tube. The vortex ring appears later ($t = 64.50$ μs). It is generated subsequently to the shock wave exiting from the shock tube, which leads to a shear layer between the external and the emerging fluids [38]. The discharge gas flow appears 1.1 ms after. When looking at the grayscale intensity profile on the aerodynamic axis time evolving (Fig. 3b), the propagation of both the vortex ring and the shock wave appears to be linear.

3.2. Image reconstruction

The reconstruction distance effects on reconstructed images are reported on Fig. 4. On a first hand, the images A, B, C and D showing the same image of drops of water and obtained for different reconstruction distances d. The area bounded around the drop is enlarged to highlight changes in the sharpness of the drop edges. On a second hand, a merit

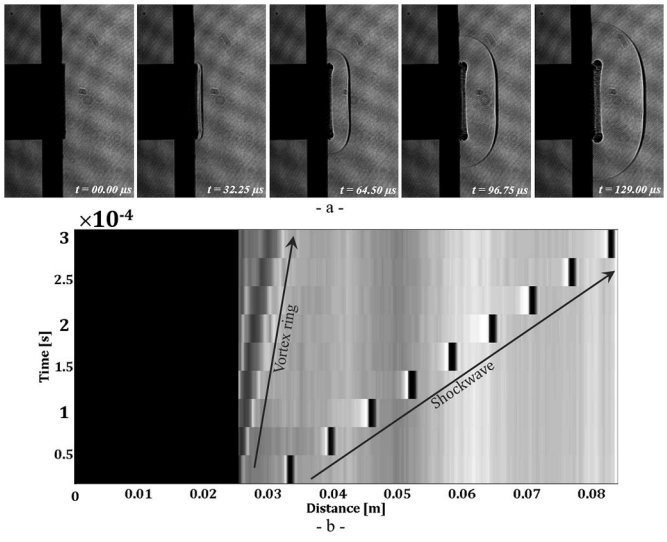

Fig. 3. a - Shadowgraphs of shock wave propagation and the vortex ring emergence. b - Grayscale intensity profile (streak image) on the aerodynamic axis representing the time propagation of the vortex ring and the shock wave.

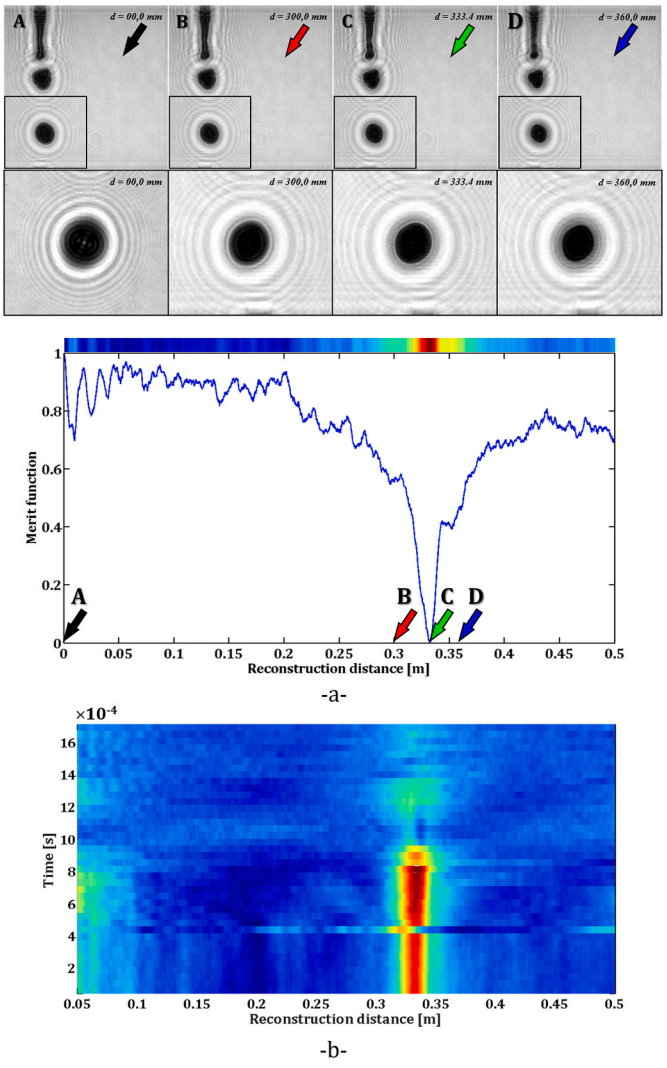

Fig. 4. Automatic determination of the focal distance: a- Drops reconstruction just before the shock wave and associated merit function, -b- Time evolution of the merit function (before and after the shock wave). The remarkable line shows the refractive effects of the shock wave.

function is calculated taken into account the whole image and fitted over a reconstruction distance d of 500.0 mm in order to identify the best reconstruction distance d_0. The latter corresponds to an optimum on the curve and for which the drop edges are shape and is in good agreement with the experimental data. All the involved reconstruction distances are reported by colored arrows on the merit function figure. A time dependence of the reconstruction distance detection is reported on Fig. 4b. The image shows that the reconstruction distance remain constant and a shift is observed in the presence of the shock wave. This shift is due to the shock overpressure that lead to local changes in the air density, and therefore local variations of the refractive index. Furthermore, after the interaction of drops with the shock, a slight broadening of the valley width giving the distance d_0 is observed. This is due to the fragmentation process that involves bigger space volume.

The image A is the one recorded on the camera sensor plane (d = 000.0 mm), C is obtained for the best reconstruction distance (d_0 = 333.4 mm) and corresponds to a minimum on our merit function figure. Although the image is well reconstructed, intensity oscillations surrounding the drops remain due to the twin image. Two main categories of approaches for the twin image elimination exist [39–46]: one based on numerical processing of reconstructed images and a second one implying changes on the hologram recording setup but are not useful in this case due to the ultrafast time evolution of the fragmentation phenomenon. The images B and D are calculated for the reconstruction distance d = 300.0 mm and d = 360.0 mm respectively, and are intermediate distances given for comparison.

3.3. Benefits of holography on fluid mechanics data survey

The experimental and theoretical investigations carried out on the aerodynamic breakup of liquid drops allowed to highlight some dimensionless key parameters involved in it description, namely the Weber number (*We*), the Ohnesorge number (*Oh*) and the Reynolds number (*Re*). The interaction of the air flow with the liquid phase of the drop is described through the Weber number which corresponds to the ratio of the aerodynamic forces to the cohesion forces of the drop. The viscosity properties of the liquid phase is characterized by the ratio viscous forces to the surface tension forces acting on the drop given by the Ohnesorge number. Finally the flow regime is quantified using the Reynolds number. The relations defining these dimensionless quantities are summarized on Table 1. It should be noted that the Ohnesorge number can be retrieved by combining both numbers *Re* and *We*. Dealing with the time scale of the breakup process, the earlier studies [47] show that a characteristic breakup time t^* which correspond to the time required for breakup to occur can be defined (Table 1).

Investigations on the aerodynamic deformation and breakup of newtonian liquids drops established that for moderate (low) Ohnesorge numbers ($Oh \lesssim 0.1$), the fragmentation phenomenon does not behave randomly, but conversely displays various distinguishable breakup regimes governed by the weber number [1]. The earliest classification attempt of the breakups regimes was proposed by Hinze in 1955 [49, 50]. Since then, several works tried to refine this breakups mode classification on the base of experimental observations [1,48,51–56]. As example, Table 2 point out the classification introduced by Pilch et *al.* [1].

The air flow and liquids parameters are summarized in Table 3. The air properties at normal temperature and pressure are $\rho_g = 1.23$ kg m^{-3} for density and $\mu_g = 18.27 \times 10^{-6}$ Pa s for the viscosity [30]. The measured average drops diameter is about $<D> = 1$ mm and the calculated Weber number *We* indicate that the sheet stripping and chaotic fragmentation regimes (catastrophic breakup) are reached ($We \geq 150$) [1,48,57]. Dealing with the flows emitted, three distinct velocities should be distinguished: The shock wave velocity v_1, the velocity v_2 of the flow field following the shock wave and velocity v_3 of the discharge gas flow (pressurized air) released after the rupture of the

Table 1
Relevant dimensionless parameters involved in the aerodynamic fragmentation [48] and characteristic breakup time [47].

Dimensionless numbers	Relationship	Parameters definition
Weber number	$We = \frac{\rho_g v_0^2 D}{\sigma}$	ρ_l: *Density of the liquid* [kg/m^3] ρ_g: *Density of the air* [kg/m^3] σ: *Surface tension of the liquid* [N.m^{-1}] v_0: *Flow velocity* [m/s] μ_l: *Dynamic viscosity of the liquid* [Pa·s] *D: Drop diameter* [m]
Ohnesorge number	$Oh = \frac{\mu_l}{\sqrt{\rho_l \sigma D}} = \frac{\sqrt{We}}{Re}$	
Reynolds number	$Re = \frac{\rho_g v_0 D}{\mu_g}$	
Characteristic breakup time	$t^* = \frac{D}{v_0}\sqrt{\frac{\rho_l}{\rho_g}}$	

Table 2

Aerodynamic fragmentation regimes [1].

Breakup modes	Weber number range
Vibrational	$We \lessapprox 12$
Bag	$12 \lessapprox We \lessapprox 50$
Bag-and-stamen	$50 \lessapprox We \lessapprox 100$
Sheet stripping	$100 \lessapprox We \lessapprox 350$
Wave crest stripping	$350 \lessapprox We$
Catastrophic (chaotic)	$350 \lessapprox We$

Table 3

Aerodynamic breakup parameters.

Quantities	Liquids		
	PEG H $(OCH_2CH_2)_nOH$	Water H_2O	Ethanol C_2H_6O
Drops diameter D [m]	1.7×10^{-3}	1.2×10^{-3}	0.95×10^{-3}
Drop deformation time [s]	7.08×10^{-4}	5.00×10^{-4}	3.75×10^{-4}
Characteristic breakup time t^* [s]	4.31×10^{-4}	3.42×10^{-4}	2.87×10^{-4}
Flow velocity v_2 [m.s^{-1}]	100	100	100
Weber number We	470	203	529
Reynolds number Re	1.13×10^4	7.98×10^3	6.32×10^3
Ohnesorge number Oh	3.26×10^{-1}	3.38×10^{-3}	9.32×10^{-3}

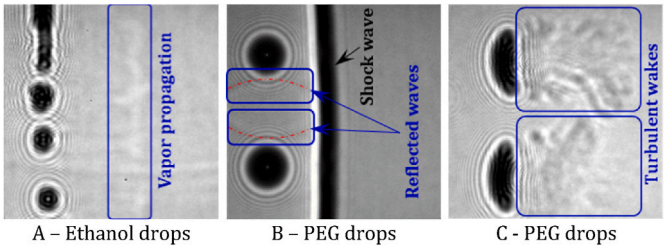

Fig. 5. Examples of recorded holograms illustrating different observable phenomena generated as a result of the interaction of a shock wave and the flow just behind with droplets. A - Ethanol vapor propagation, B - Shock wave reflections (dashed red lines) by PEG droplets, C - Turbulent wake behind PEG deforming droplets.

aluminum foils (rupture disk). At the scale time of the fragmentation process, only the shock wave and the flow field just behind are involved. Related velocities v_1 and v_2 are extracted from the shadowgraphs and the digital holography images.

Through the calculation of the Reynolds numbers (Table 3) for the air flow acting around the initial drops which exhibits a sphere-like shape, it is possible to qualify the wake stream behind the drops. Therefore, the achieved order of magnitude of 10^3–10^4 for *Re* values (Table 3) show that air flow is turbulent and should display vortices on it stream [30]. These vortices and turbulence are clearly emphasized in our current experimental digital holography work for the case of polyethylene glycol deforming drops (Figs. 5 and 6). The vortices are generated backward the drops and drift downstream in wake flow. The airstream turbulence evidence might be improved by the use of shadowgraph visualization technique.

The investigated liquids are chosen owning their physico-chemical properties that include the volatility and the viscosity. The ethanol being the most volatile liquid (Boiling point: 78.5 °C) and the PEG the most viscous. Viscosity effects of the drops are quantified through the Ohnesorge number. Table 3 shows that the low *Oh* values achieved ($Oh \lessapprox 0.1$) are associated with liquids having a moderate viscosity [58]. The fragmentation process, is therefore mainly governed by the Weber

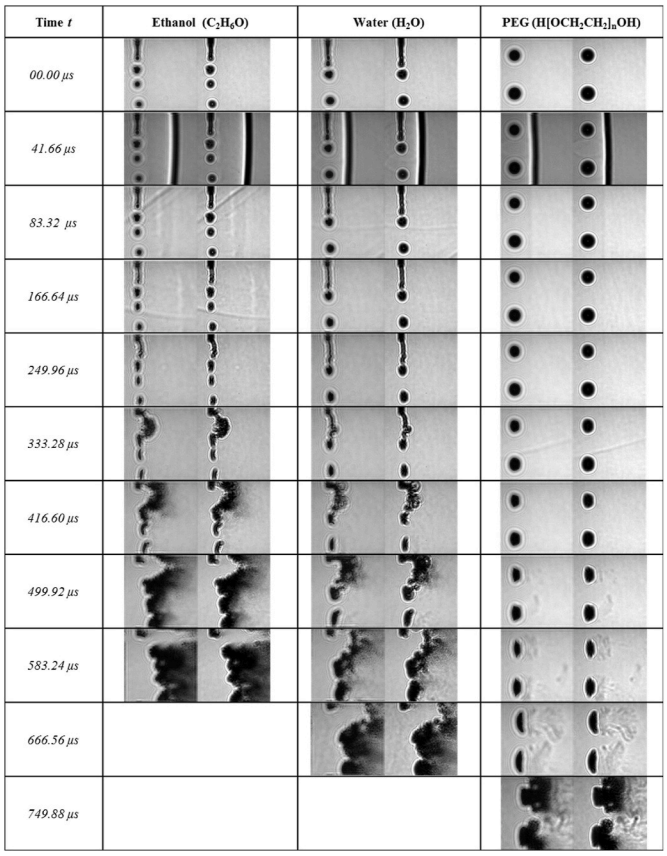

Fig. 6. Time evolution of the aerodynamic fragmentation of ethanol, water and polyethylene glycol liquids.

number. The ability of a drop to deform and breakup will weaken for large Ohnesorge number values since the damping is increased by the viscous forces of the liquid [59]. For both solutions of ethanol and water, the *Oh* values are in the order of magnitude of 10^{-3} stress less damping whereas for the case of the PEG solution which is more viscous, $Oh \sim 10^{-1}$ emphasize a reduced sensitivity to aerodynamic forces and a damped deformation.

Interestingly, the digital in-line holography experimental setup offers not only the opportunity to reconstruct the drops, characterize and locate them in the 3D free space, but also give the possibility of highlighting others fluid mechanics phenomena (Fig. 5) such as the generation and propagation of vapors subsequent to the interaction of ethanol drops with a shock wave, reflections by the PEG drops of the wave of shock, and the turbulent wake behavior of the air flow backward deforming PEG drops. Indeed, in-line digital holography acts like a shadowgraphy configuration but with an infinite focus.

The time evolution of the aerodynamic fragmentation processes of ethanol, water and polyethylene glycol droplets are reported in Fig. 6. Liquids are sorted by columns from left to right by increasing density values. Each image is composed of 2 parts: the amplitude of the reconstructed field at the best reconstruction plane on the left side and the recorded hologram on the right side. As convention, the flow moves from left to right. The time scale origin is set just before the interaction of the shock wave with the drops where all drops exhibits a spherical like-shape. At $t = 41.65$ µs the shock wave appears, it consists of a black and white band that reflects the density variation within it. It is a refraction of the incident light beam from the dark region to the white one. Immediately after the crossing of the drops by the shock wave, reflections are observed in the surrounding of the drops for both water and PEG solution. Furthermore, for the drops of PEG, when deform passing from a sphere to a disk, the drag forces increase leading to visible

turbulences in its wake (t = 416.60 μs to t = 666.56 μs) just before its fragmentation. The results show that the shock wave overpressure of few hundred mbar effects on the drops appears to be negligible. Nevertheless, there is a removal of matter in the form of steam for the volatile compounds as shown for the case of the ethanol with a white drag (ethanol vapor) in the wake of the shock wave (at t = 83.32 μs and t = 166.64 μs). The generated vapor propagation velocity was extracted from the pictures and was found to be 1.769 m s^{-1}. In the risks field, such removal of matter in vapor form constitutes a critical situation as it can promote combustion.

In all cases, the main contribution to the fragmentation process is attributable to flow field following the shock wave. The drops deformations before fragmentation occurs in less than 1 ms (Table 1). This time scale is consistent with the characteristic breakup time t^* (Table 1) defined by Ranger and Nicholls [47]. These times could be reduced for higher overpressures. The breakup process for involved liquids are likely similar: The leeward face of the drop are firstly flattened. There is a radial transfer of matter moves from the center of the leeward side towards its periphery under the effect of the aerodynamic forces, and then detaches in the form of flatten ring which breaks down (PEG at t = 749.88 μs). This removal of matters is accomplished in a cyclic way.

An additional foremost importance phenomenon involved in the aerodynamic fragmentation of drops is the interface instabilities. Such surface disturbances are amplified by aerodynamic effects. Three types of instabilities that may occur are reported in the literature, namely: Rayleigh-Taylor (RT), Kelvin-Helmholtz (KH) and Richtmyer-Meshkov (RM) instabilities. The Richtmyer-Meshkov instabilities [60–63] arise when the local density gradient at the interface of the drop and the pressure gradient of the shock are misaligned. It occur during the interaction between the shock wave with the surface of the drop. Rayleigh-Taylor instabilities [48,64–66] arise when a density discontinuity is accelerated toward the lower density. They are assumed to occur at the forward or rear stagnation points. Kelvin-Helmholtz instabilities [67,68] occur when high relative velocities exist at an interface. They occur at the periphery of the drop where the largest relative velocity between the drop and ambient are observed. However, due to the large accelerations experienced by the drop, most authors have assumed RT instabilities dominate and control the catastrophic breakup mode. By analyzing our experimental results of the aerodynamic breakup, the shock wave interaction with the drops of the 3 liquids didn't exhibit visible disturbances. Although, the absence of changes may be related to the weak amplitude of the shock wave, in their early work, Ranger and Nicholls [47] reported that the impact of a strong shock wave on a liquid drop is not significant for the shattering of the drop and it main role is to produce high speed convective flow which is responsible for it breakup. Our results show the fattening of the windward surface of drops and the appearance of some wrinkles [69] on the rear surface. To evidence these instabilities and their effects, further analyses still have to be performed using others visualization techniques as the Laser Induced Fluorescence (LIF) exploited by Theofanous et *al.* [70,71] to investigate the surface flows or the shadowgraphy technique to probe internal flows through the density changes.

4. Conclusion

A lab-made open-ended shock tube was constructed and fully characterized by high-speed imaging shadowgraphy and ultrafast pressure measurements. The investigation of the aerodynamics fragmentation process of the ethanol, ultrapure water and polyethylene glycol 300 millimetric diameter drops by high speed digital in-line holography, emphasized complex behaviors which depend upon the physico-chemical properties of the liquids. The obtained results evidenced phenomena related to the interaction of both the shock wave and the flow just behind it with the drops, such as vapor cloud generation and propagation for ethanol, shock wave reflection by the drops, and turbulences with vortices propagation downstream of the drops. The liquids droplets aerodynamic breakup occur in 'chaotic regime' and are consistent with the description reported by Pilch and Erdman. The dense particle cloud created by fragmentation is currently under study. The shock wave impact effects upon the drops still unclear as it didn't show visible surface disturbances related to the instabilities. Such results may be related to the low amplitude of the shock wave, and require the use of further visualization techniques to investigate both internal and interfacial changes (LIF, shadowgraphy).

Credit author statement

Each author has been involved in the design of the study, interpretation of the data, and writing of the manuscript. Each of the authors has read and concurs with the content in the manuscript.

Declaration of competing interest

The authors declare that they have no known competing financial interests or personal relationships that could have appeared to influence the work reported in this paper.

Acknowledgments

The authors would like to thank Christian Lopez from Laboratoire des Sciences des Risques (LSR), IMT Mines Alès, for technical support and Fabrice Lamadie from CEA Marcoule for fruitful discussions.The authors are also grateful to Nicolas Long from Trinoma (France) for the ultra-fast imaging support.

References

[1] M. Pilch, C.A. Erdman, Use of breakup time data and velocity history data to predict the maximum size of stable fragments for acceleration-induced breakup of a liquid drop, Int. J. Multiphas. Flow 13 (1987) 741–757.
[2] F. Olchewsky, Z. Essaïdi, J.M. Desse, F. Nicolas, F. Champagnat, P. Picart, 3D gas density reconstruction by digital holographic interferometry, Opt. InfoBase Conf. Pap. Part F47-D (2017) 5–7.
[3] J.M. Desse, P. Picart, P. Tankam, Digital color holography applied to fluid and structural mechanics, Opt Laser. Eng. 50 (2012) 18–28.
[4] Pascal Picart, New Techniques in Digital Holography, 2015.
[5] J. Katz, J. Sheng, Applications of holography in fluid mechanics and particle dynamics, Annu. Rev. Fluid Mech. 42 (2010) 531–555.
[6] D. Gabor, A new microscopic principle, Nature 161 (1948) 777–778.
[7] M.K. Kim, Digital Holographic Microscopy, Springer-Verlag New York, 2011.
[8] E.N. Leith, J. Upatnieks, Reconstructed wavefronts and communication theory, J. Opt. Soc. Am. 52 (1962) 1123–1130.
[9] P. Lauret, F. Heymes, P. Slangen, L. Aprin, N. Lecysyn, Consequences of liquid jet breakup resulting from interaction with overpressure wave from domino effect, Chem. Eng. Trans. 53 (2016) 73–78.
[10] F. Heymes, L. Aprin, P. Slangen, E. Lapébie, A. Osmont, G. Dusserre, On the effects of a triple aggression (fragment, blast, fireball) on an LPG storage, Chem. Eng. Trans. 36 (2014) 355–360.
[11] W. Merzkrich, Flow Visualization, Academic Press, 1987.
[12] G.S. Settles, Schlieren and Shadowgraph Techniques, Springer, Berlin, Heidelberg, 2001.
[13] J.H. Gladstone, T.P. Dale, Researches on the refraction , dispersion , and sensitiveness of liquids, Phil. Trans. Roy. Soc. Lond. 153 (1863) 317–343.
[14] B.J. Breckinridge, George D. Voelz, Computational Fourier Optics, SPIE Press, 2011.
[15] J.A. Ratcliffe, Some aspects of diffraction theory and their application to the ionosphere, Rep. Prog. Phys. 19 (1956) 188–267.
[16] J.w. Goodman, Introduction to Fourier Optics, Third, Roberts and Company Publishers, 2005.
[17] U. Schnars, W.P.O. Jüptner, Digital recording and numerical reconstruction of holograms This, Meas. Sci. Technol. 13 (2002) R85–R101.
[18] J. Gillespie, R.A. King, The use of self-entropy as a focus measure in digital holography, Pattern Recogn. Lett. 9 (1989) 19–25.
[19] Z. Ren, N. Chen, E.Y. Lam, Extended focused imaging and depth map reconstruction in optical scanning holography, Appl. Opt. 55 (2016) 1040–1047.
[20] P. Langehanenberg, B. Kemper, D. Dirksen, G. Von Bally, Autofocusing in Digital Holographic Phase Contrast Microscopy on Pure Phase Objects for Live Cell Imaging, 2008.
[21] M.L. Tachiki, M. Itoh, T. Yatagai, Simultaneous depth determination of multiple objects by focus analysis in digital holography, Appl. Opt. 47 (2008) D144–D153.
[22] F. Dubois, C. Schockaert, N. Callens, C. Yourassowsky, Focus plane detection criteria in digital holography microscopy by amplitude analysis, Opt Express 14 (2006) 5895.

[23] S. Grare, D. Lebrun, S. Coëtmellec, M. Brunel, G. Perret, G. Gréhan, Dual wavelength digital holography for 3D Particle Image Velocimetry: application to vortex dynamics, Opt. InfoBase Conf. Pap. 15009 (2016) 2–6.
[24] E.S.R. Fonseca, P.T. Fiadeiro, M. Pereira, A. Pinheiro, Comparative analysis of autofocus functions in digital in-line phase-shifting holography, Appl. Opt. 55 (2016) 7663.
[25] S.K. Mohammed, L. Bouamama, D. Bahloul, P. Picart, Quality assessment of refocus criteria for particle imaging in digital off-axis holography, Appl. Opt. 56 (2017) F158.
[26] T. Yeo, S. Ong, Jayasooriah, R. Sinniah, Autofocusing for tissue microscopy, Image Vis Comput. 11 (1993) 629–639.
[27] L. Firestone, K. Cook, K. Culp, N. Talsania, K. Preston, Comparison of autofocus methods for automated microscopy, Cytometry 12 (1991) 195–206.
[28] D. Vollath, Automatic focusing by correlative methods, J. Microsc. 147 (1987) 279–288.
[29] H.J.J. Staat, A. van der Bos, M. van den Berg, H. Reinten, H. Wijshoff, M. Versluis, D. Lohse, Ultrafast imaging method to measure surface tension and viscosity of inkjet-printed droplets in flight, Exp. Fluid 58 (2017) 1–8.
[30] A.K. Flock, D.R. Guildenbecher, J. Chen, P.E. Sojka, H.J. Bauer, Experimental statistics of droplet trajectory and air flow during aerodynamic fragmentation of liquid drops, Int. J. Multiphas. Flow 47 (2012) 37–49.
[31] Sigma Aldrich. https://www.sigmaaldrich.com.
[32] F.G. Friedlander, The diffraction of sound pulses; diffraction by a semi-infinite plane, Proc. R. Soc. Lond. A. Math. Phys. Sci. 186 (1946) 322–344.
[33] A.F. Tasissa, M. Hautefeuille, J.H. Fitek, R.A. Radovitzky, On the formation of Friedlander waves in a compressed-gas-driven shock tube, Proc. R. Soc. A Math. Phys. Eng. Sci. 472 (2016).
[34] A. Sundaramurthy, N. Chandra, A parametric approach to shape field relevant blast wave profiles in compressed gas-driven shock tube, Front. Neurol. 5 (2014) 1–10.
[35] A.J. Newman, J.C. Mollendorf, The peak overpressure field resulting from shocks emerging from circular shock tubes, J. Fluids Eng. Trans. ASME 132 (2010) 2–8.
[36] W. Bleakney, D.K. Weimer, C.H. Fletcher, The shock tube: a facility for investigations in fluid dynamics, Rev. Sci. Instrum. 20 (1949) 807–815.
[37] N. Chandra, S. Ganpule, N.N. Kleinschmit, R. Feng, A.D. Holmberg, A. Sundaramurthy, V. Selvan, A. Alai, Evolution of blast wave profiles in simulated air blasts: experiment and computational modeling, Shock Waves 22 (2012) 403–415.
[38] K. Kontis, R. An, U. Kingdom, J.A. Edwards, U. Kingdom, I. Introduction, Compressible Vortex-Ring Interaction Studies with a Number of Generic Body Con Fi Gurations, vol. 44, 2006.
[39] L. Denis, C. Fournier, T. Fournel, C. Ducottet, Numerical suppression of the twin image in in-line holography of a volume of micro-objects, Meas. Sci. Technol. 19 (2008).
[40] E.N. Leith, J. Upatnieks, Wavefront reconstruction with continuous-tone objects, J. Opt. Soc. Am. 53 (1963) 1377–1381.
[41] E. Cuche, P. Marquet, C. Depeursinge, Spatial filtering for zero-order and twin-image elimination in digital off-axis holography, Appl. Opt. 39 (2000) 4070.
[42] I. Yamaguchi, T. Zhang, Phase-Shifting digital holography, Opt. Lett. 22 (1997) 1268–1270.
[43] T. Latychevskaia, H.W. Fink, Solution to the twin image problem in holography, Phys. Rev. Lett. 98 (2007) 1–4.
[44] G. Koren, F. Polack, D. Joyeux, Twin-image elimination in in-line holography of finite-support complex objects, Opt. Lett. 16 (1991) 1979–1981.
[45] G. Koren, F. Polack, D. Joyeux, Iterative algorithms for twin-image elimination in in-line holography using finite-support constraints, J. Opt. Soc. Am. A 10 (1993) 423–433.
[46] G. Pedrini, P. Fröning, H. Fessler, H.J. Tiziani, In-line digital holographic interferometry, Appl. Opt. 37 (1998) 6262.
[47] A.A. Ranger, J.A. Nicholls, Aerodynamic shattering of liquid drops, AIAA J. 7 (1969) 285–290.
[48] D.R. Guildenbecher, C. López-Rivera, P.E. Sojka, Secondary atomization, Exp. Fluid 46 (2009) 371–402.
[49] J.O. Hinze, Fundamentals of the hydrodynamic mechanism of splitting in dispersion processes, AIChE J. 1 (1955) 289–295.
[50] Efstathios Michaelides, C.T. Crowe, J.D. Schwarzkopf, Multiphase Flow Handbook, second ed., CRC Press, 2016.
[51] S.A. Krzeczkowski, Measurement of liquid droplet disintegration mechanisms, Int. J. Multiphas. Flow 6 (1980) 227–239.
[52] L.P. Hsiang, G.M. Faeth, Drop deformation and breakup due to shock wave and steady disturbances, Int. J. Multiphas. Flow 21 (1995) 545–560.
[53] Z. Dai, G.M. Faeth, Temporal properties of secondary drop breakup in the multimode breakup regime Z, Int. J. Multiphas. Flow 27 (2001) 217–236.
[54] H. Zhao, H.F. Liu, W.F. Li, J.L. Xu, Morphological classification of low viscosity drop bag breakup in a continuous air jet stream, Phys. Fluids 22 (2010).
[55] M. Jain, R.S. Prakash, G. Tomar, R.V. Ravikrishna, Secondary breakup of a drop at moderate Weber numbers, Proc. R. Soc. A Math. Phys. Eng. Sci. 471 (2015).
[56] W. Yang, M. Jia, Z. Che, K. Sun, T. Wang, Transitions of deformation to bag breakup and bag to bag-stamen breakup for droplets subjected to a continuous gas flow, Int. J. Heat Mass Tran. 111 (2017) 884–894.
[57] T. Kékesi, G. Amberg, L. Prahl Wittberg, Drop deformation and breakup, Int. J. Multiphas. Flow 66 (2014) 1–10.
[58] G. Strotos, I. Malgarinos, N. Nikolopoulos, M. Gavaises, Predicting droplet deformation and breakup for moderate Weber numbers, Int. J. Multiphas. Flow 85 (2016) 96–109.
[59] L.P. Hsiang, G.M. Faeth, Near-limit drop deformation and secondary breakup, Int. J. Multiphas. Flow 18 (1992) 635–652.
[60] R.D. Richtmyer, Taylor instability in shock acceleration of compressible fluids, Commun. Pure Appl. Math. 13 (1960) 297–319.
[61] E.E. Meshkov, Instability of the interface of two gases accelerated by a shock wave, Fluid Dynam. 4 (1969) 101–104.
[62] M. Brouillette, The richtmyer-meshkov instability, Annu. Rev. Fluid Mech. 34 (2002) 445–468.
[63] Y. Zhou, Rayleigh–Taylor and Richtmyer–Meshkov instability induced flow, turbulence, and mixing. II, Phys. Rep. 723–725 (2017) 1–160.
[64] G. Taylor, The instability of liquid surfaces when accelerated in a direction perpendicular to their planes. I, Proc. R. Soc. London. Ser. A. Math. Phys. Sci. 201 (1950) 192–196.
[65] Strutt J.W. Rayleigh, Investigation of the character of the equilibrium of an incompressible heavy fluid of variable density, Proc. Lond. Math. Soc. 14 (1883) 170–177.
[66] D.D. Joseph, J. Belanger, G.S. Beavers, Breakup of a liquid drop suddenly exposed to a high-speed airstream, Int. J. Multiphas. Flow 25 (1999) 1263–1303.
[67] W.T. Kelvin, Hydrokinetic solutions and observations, London, Edinburgh, Dublin Philos. Mag. J. Sci. 42 (1871) 362–377.
[68] H. Von Helmholtz, On discontinuous movements of fluids, London, Edinburgh, Dublin Philos. Mag. J. Sci. 36 (1868) 337–346.
[69] X.Y. Yi, Y.J. Zhu, J.M. Yang, T. Wang, M.Y. Sun, Rear-surface deformation of a water drop in aero-breakup of shear mode, Chin. Phys. Lett. 34 (2017) 1–4.
[70] G.T. Theofanous, J.G. Li, On the physics of aerobreakup, Phys. Fluids 20 (2008).
[71] T.G. Theofanous, Aerobreakup of Newtonian and viscoelastic liquids, Annu. Rev. Fluid Mech. 43 (2011) 661–690.